Sensing a Connection: Tree Distribution is Influenced by Deep Critical Zone Structure

B. A. Flinchum[1], C. J. Harman[2,3], and D. Hagan[4]

[1]School of Civil and Environmental Engineering and Earth Sciences, Clemson University, Clemson, South Carolina, USA

[2]Department of Environmental Health and Engineering, Johns Hopkins University, Baltimore, Maryland, USA

[2]Department of Earth and Planetary Sciences, Johns Hopkins University, Baltimore, Maryland, USA

[4]Department of Forestry and Environmental Conservation, Clemson University, Clemson, South Carolina, USA

.

Corresponding author: Brady Flinchum (bflinch@clemson.edu)

Key Points:

- Canopy heights in a headwater watershed increase when regolith thins.
- The presence of quaking aspen in arid/semi-arid environments of the Rocky Mountain region might be an indication of shallow bedrock.
- Shallow bedrock impacts groundwater flow, creating ideal conditions for trees requiring high water volumes in well-drained soils.

Abstract

This study explores the impact of deep (>5 m) critical zone (CZ) architecture on vegetation distribution in a semi-arid snow-dominated climate. Utilizing seismic refraction surveys, we identified a significant correlation between saprolite thickness and LiDAR-derived canopy heights (R^2=0.47). We argue that CZ structure, specifically shallow fractured bedrock under valley bottoms, redirects groundwater to locations where trees are established—suggesting they are located in specific locations with access to nutrients and water. This work provides a unique spatially exhaustive perspective and adds to growing evidence that in addition to other factors such as slope, aspect, and climate, deep CZ structure plays a vital role in ecosystem development and resilience.

Plain Language Summary

This study investigates how the hidden structure beneath the Earth's surface (called the critical zone or CZ) affects where plants can grow and thrive. Using seismic refraction surveys, we found that the critical zone structure correlates with tree distribution. Specifically, areas with shallow fractured bedrock support the tallest trees. We argue that the shape of the critical zone forces groundwater toward the surface, providing a steady water supply for trees during spring and late summer. Our 1.5 km of seismic refraction data reveal a consistent pattern: trees are taller when the fractured bedrock is close to the surface. This connection suggests that the influence of critical zone structures on vegetation distribution in a given landscape may be as significant as other factors such as slope, aspect, and climate.

1 Introduction

The critical zone (CZ) is the region near the Earth's surface created and maintained by complex interactions between the atmosphere, hydrosphere, and biosphere, and spans from the top of the canopy to fresh bedrock (S. L. Brantley et al., 2005; Susan L. Brantley et al., 2007). In the CZ, rock is transformed into soil by physical and chemical weathering processes (Susan L Brantley, 2010; Gu et al., 2020; Lebedeva et al., 2007). This transformation releases critical nutrients for plants and ecosystems (Arvin et al., 2017; Hahm et al., 2014; Uhlig et al., 2017; Uhlig & Blanckenburg, 2019) while providing porosity for groundwater storage (Graham et al., 1997; Hayes et al., 2019; Navarre-Sitchler et al., 2015). Here, we demonstrate evidence that deep (>5 m) CZ architecture impacts the distribution of vegetation in semi-arid headwater watersheds by influencing groundwater storage and flow.

This study was motivated by a clear and distinct pattern in vegetation visible in the Laramie Range, just southeast of Laramie, Wyoming (Figure 1). This part of the Laramie Range, classified as a semiarid rangeland, sits at an elevation between 2200 and 2700 m. The low-lying areas are dominated by willows (*Salix* spp.), aspens (*Populus* spp.), and meadow grasses (Carey et al., 2019; Carey & Paige, 2016). Aerial photographs provided by the National Agriculture Imagery Program (NAIP) from July 2022 highlight the distinct vegetation patterns (Figure 1a). In general, north-facing slopes tend to have more vegetation, and many of the first-order drainages appear to support thick stands of vegetation (Figure 1a). However, not all first-order drainages exhibit dense vegetation, suggesting another process might be important in vegetation distribution across this landscape (Figure 1).

Previous studies have examined relationships between vegetation density and surface topographic attributes such as slope, aspect, and relief (Emanuel et al., 2014; Gillieson et al.,

1996; Marston, 2010). However, few have examined the role of subsurface topography. Here, we use shallow seismic refraction surveys to characterize relationships between vegetation density and deep CZ structure. Seismic refraction surveys generate profiles of seismic velocity tens of meters deep and hundreds to thousands of meters long (Flinchum et al., 2022; Uecker et al., 2023). The strong relationship between seismic velocity and porosity means these images can indicate the depth and degree of weathering in landscapes underlain by crystalline bedrock (Callahan et al., 2020; Hayes et al., 2019; Holbrook et al., 2014). In recent years, seismic refraction has allowed CZ architecture to be characterized over large spatial scales in various lithologies and climates (Donaldson et al., 2023; Huang et al., 2021; Leone et al., 2020; Pedrazas et al., 2021).

The seismic refraction velocities presented here are correlated with vegetation height (R^2=0.47), suggesting a connection between existing CZ structure and the distribution of trees. We hypothesize that the shallow bedrock under the tallest canopy forces groundwater to the surface under these drainages. The presence of shallow fractured bedrock prevents water loss during the spring melt and redirects older water from higher in the watershed into the valley bottoms, providing a reservoir of water and nutrients for the trees throughout the growing season.

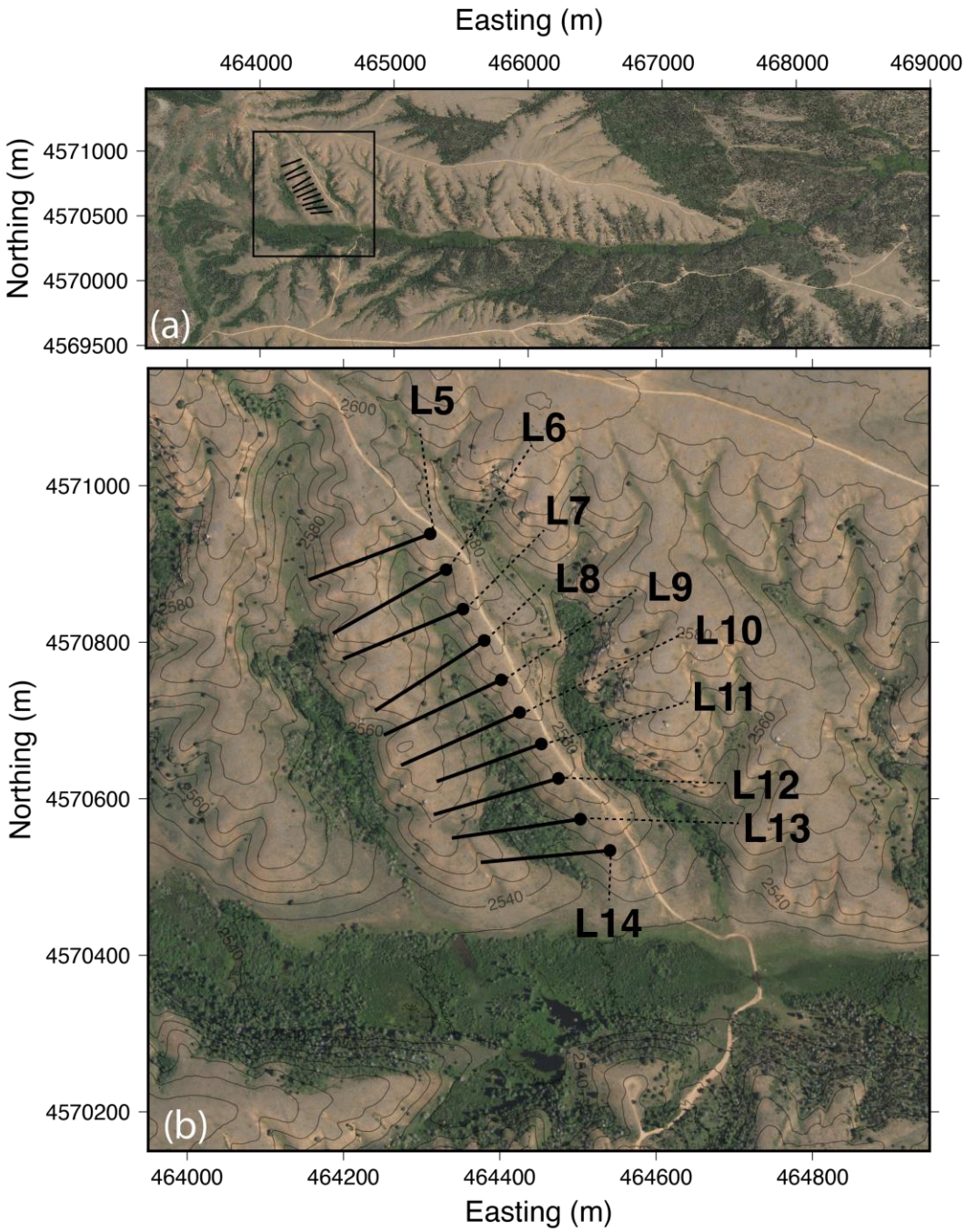

Figure 1 Map of the study area. The image is an aerial photograph from the National Agricultural Image Program (NAIP) taken on July 2, 2022, and topographic contours are derived from 1 m LiDAR data. Dots are the start of seismic profiles.

2 Materials and Methods

2.1 Study Site

We collected 1.5 km of seismic refraction data in a small North/South trending valley (which we will refer to as V1) defined by interfluves with approximately 20 m of relief (Figure 1a). V1 has an ephemeral stream and drains into North Lodgepole Creek, a perennial stream with numerous beaver ponds along its reach, flowing approximately east-west in our study area (Figure 1a). There is a notable stand of quaking aspen trees (*Populus tremuloides* Michx.) at the outlet of V1 (Figure 1b). As the valley climbs in elevation, the trees give way to shrub-steppe and grassland vegetation. In the Laramie Range, these isolated and patchy stands of trees persist, whereas another stand exists in the valleys to the east and the west (Figure 1b). Given the patchiness of the vegetation, we set up geophysical surveys to determine if the locations of the trees were associated with the CZ structure.

The study site is part of a gentle undulated topography on the Rocky Mountain erosional surface (Chapin & Kelley, 1997; Eggler et al., 1969; Evanoff, 1990). Erosion rates from cosmogenic nuclides suggest that this surface erodes at a rate that will replace the gently rolling hills every 1 to 2 million years (Dethier et al., 2014). The NLC site is non-glaciated granitic terrain and relatively undisturbed by human land use. Ten years of local climate data from the Crow Creek SNOTEL station (~2 km south) show the site has a mean annual temperature of 5.4 °C and receives 620 mm of annual precipitation, where 90% of the precipitation is recorded as snow (Natural Resources Conservation Service (NRCS), 2015).

There are two well-known study sites nearby where we can leverage existing observations. The Three Little Valleys site is 5 km south of the NLC site and is of the same geology with similar, distinct asymmetrical slopes and vegetation cover (Uecker et al., 2023).

Despite the apparent asymmetrical contrast, Uecker et al. (2023) collected 3.9 km of seismic refraction data and showed that the depth to bedrock could be greater than 60 m and argued that trees on the north-facing slopes are preferentially located to obtain more water based on differences in P-wave velocity (Uecker et al., 2023). Another well-studied site is the Blair-Wallis (BW) located 12 km south (Flinchum, Holbrook, Grana, et al., 2018; Flinchum et al., 2019; Keifer et al., 2019; Pasquet et al., 2021; Wang et al., 2019). At BW, the CZ was reported to be upwards of 60 m thick under ridges but only 2-3 m thick under valley bottoms. At BW, inverted bedrock topography was observed and fits well with a regional stress model under regional compressive stress (Flinchum, Holbrook, Rempe, et al., 2018).

2.2 Seismic Refraction

The seismic profiles presented were acquired in 2015 using Geometrics Geodes and 144 or 168 geophones at 1-meter spacing. Shots were collected using a sledgehammer, and the spacing varied between 5 and 10 meters. Each shot was stacked 5 and 8 times to increase the signal to noise. Topographic profiles were extracted from 1-meter resolution LiDAR data collected by the Wyoming Center for Hydrology and Environmental Geophysics (WyCEHG) in 2014.

We manually picked the first arrivals in Python. We were conservative, omitting channels where the first arrival was unclear. Most of the arrivals were picked without a filter. However, a band-pass filter (20-150 Hz) was used to pick the farthest offset arrivals. We used reciprocal travel times to ensure we picked the same phase of the first arrival. We used the refraction package in the Python Geophysical Inversion Modeling Library (PyGIMLi) to invert the first arrival times (Rücker et al., 2017). The forward model assumes the elastic energy travels as rays.

This assumption allows the package to use a computationally efficient shortest path algorithm (Dijkstra, 1959; T. Moser, 1991; T. J. Moser et al., 1992). The inversion uses a deterministic Gauss-Newton scheme that minimizes the $\chi 2$ error. To compute the $\chi 2$ error, every arrival time must have an associated uncertainty value. These assigned uncertainty values have a large weight in the final solution. Here, we assigned uncertainties using a linear interpolation based on the distance between the source and the receiver. At small offsets, we assign a small uncertainty (~1 ms); at larger offsets, we assign a larger uncertainty (~3 ms). This interpolation of the uncertainty emphasizes our ability to better pick arrivals from near offsets because of signal-to-noise in the data (B. Flinchum et al., 2021; B. A. Flinchum et al., 2020).

3 Results

3.1 Seismic Refraction

The velocities in the profiles increase from the top to the bottom of the V1 watershed (e.g., north to south) (Figure 2). In the upper parts of the watershed, the profiles are characterized by low (Vp < 1200 m/s) seismic velocities that extend greater than 20 m into the subsurface (Figure 2). In our data set, it is rare to encounter velocities greater than 3000 m/s. L10 is the only profile that shows velocities greater than 4000 m/s (Figure 2). The highest velocities in L10 occur at the valley bottom. However, they are slightly offset to the west relative to the center of the drainage and have an asymmetrical shape with an apparent dip to the west. Moving further south and closer to the exit of the watershed, the velocities never exceed 4000 m/s, but the high-velocity anomaly (Vp > 3000 m/s) comes closer to the surface while spanning the valley bottom (Figure 2).

L13 shows there is a recognizable shift in subsurface structure, where the high velocities (Vp > 3000 m/s) come close (<1-2 m) to the surface and then stay present for approximately 75 m (Figure 2). On L13, the sharp lateral gradients remain sharp on the east but also become well-defined and sharp on the west (Figure 2). On L14, the high-velocity region weakens, but the asymmetry switches directions. Hence, the high-velocity anomaly appears to dip to the east and is bound to the west by a lateral gradient while the east gently tapers off (Figure 2). L10, the one with the highest velocities, marks the onset of the stand of trees. The stand of trees spans the entire valley at the same location where the high-velocity anomaly is the shallowest and most continuous on the surface along L13 (Figure 2). The spatial plots illustrate that the northernmost profiles lose the higher velocities but also get slower, where velocities greater than 1200 m/s are almost absent on the northernmost profile (L5).

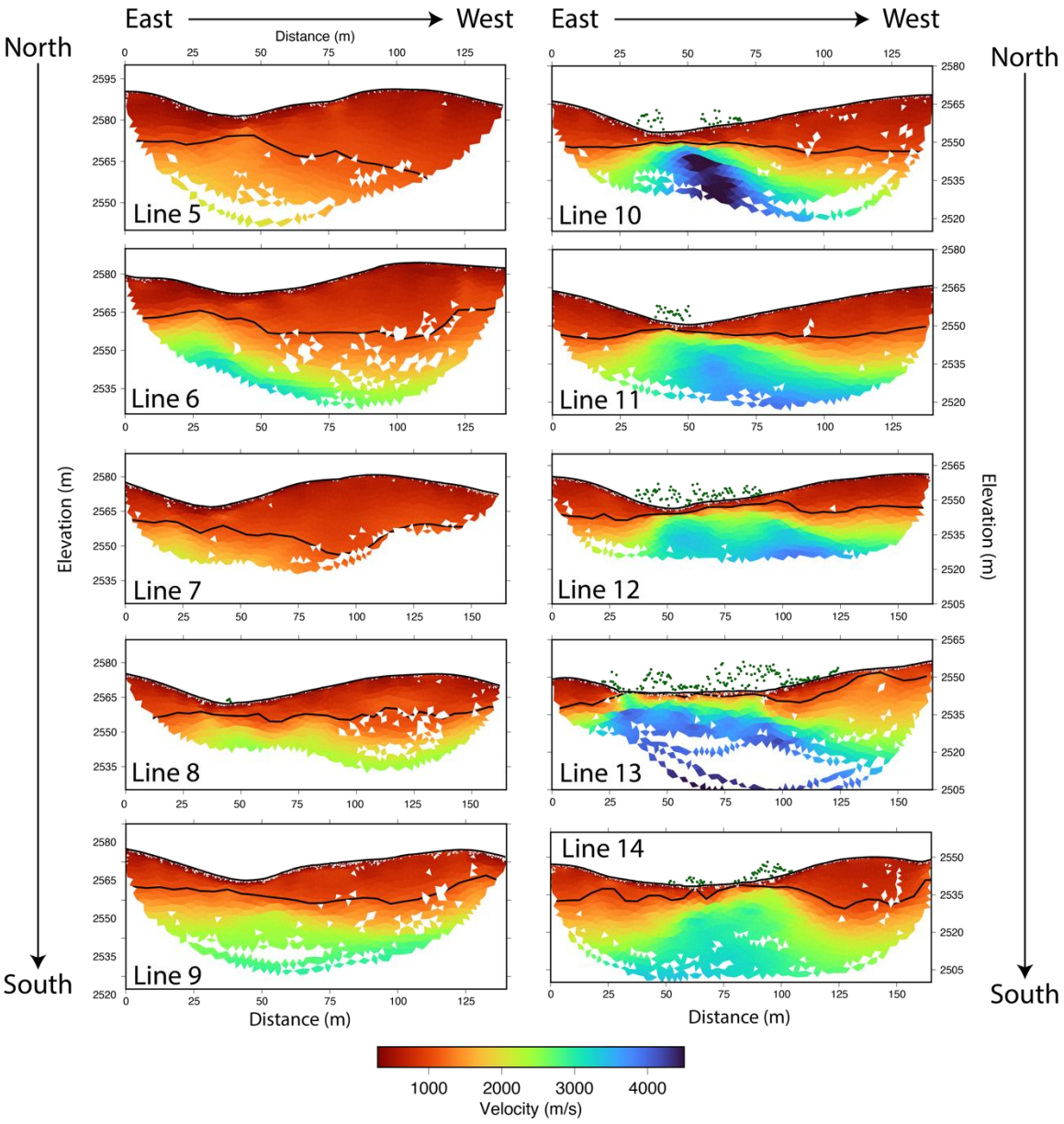

Figure 2 Seismic refraction results for all profiles in the first-order drainage. All profiles are masked by ray coverage. The solid black line plotted in each profile is the 1200 m/s contour. Green dots are extracted from the vegetation heights at 1 m resolution. The profiles are organized from north (Line 5) to south.

3.2 Saproilte Thickness and Canopy Heights

Boreholes and soil pits were not available to interpret the seismic velocities, so we rely on results from BW (Flinchum et al., 2019; Flinchum, Holbrook, Grana, et al., 2018; Keifer et al., 2019; Pasquet et al., 2021; Wang et al., 2019). At BW, 13 Geoprobe and deep wells were drilled, and the depth of refusal of the Geoprobe or the casing depth of the larger holes occurred at a velocity of 1100 +/- 180 m/s (mean and standard deviation) (Flinchum, Holbrook, Grana, et al., 2018; Flinchum, Holbrook, Rempe, et al., 2018). Since our site is in a similar climate on the same lithology, we interpret the 1200 m/s velocity contour to mark the bottom of the saprolite. Seismic refraction profiles conducted on granites in the Laramie Range (Flinchum, Holbrook, Rempe, et al., 2018) and Southern Sierra Nevada Mountains (Holbrook et al., 2014) show that unfractured bedrock should have a velocity of ~4000 m/s.

We extracted the depth to 1200 m/s along each profile to mark the boundary divding saprolite and fractured rock. Then, we used a continuous curvature spline (Smith & Wessel, 1990) to construct a saprolite thickness map of a rectangular region around our profiles (Figure 3a). The data were interpolated to a 5x5 meter grid. We applied a 7 m Gaussian smoothing filter to the vegetation height to smooth out the canopy (Figure 3b) and interpolated the smooth canopy heights to a 5x5 meter grid to investigate the visible correlations between saprolite thickness and canopy height (Figure 3c). The interpolated saprolite thickness maps show that the saprolite thins as the trees get taller (Figure 3). The relationship with the canopy height appears to be a power relationship (a = 4.72; b = -0.46) with a stronger negative correlation in log-log space as opposed to linear space ($R_{log\text{-}log}$ = -0.68 versus R_{linear} = -0.60) (Figure 3). The stand of trees is tallest along L11, L12, and L13, and, vegetation taller than 5 m is present on L10 through L14. The saprolite starts to thin at L10, which marks the onset of the large stand of trees. The

thinnest saprolite occurs along L13 and is less than 2 m thick for over 75 m along the valley bottom, which is also the widest and tallest location where the trees are usually greater than 7-8 m tall (Figure 3).

Our seismic refraction data in V1 rarely encounter velocities greater than 4000 m/s (Figure 2). This is anomalous because TLV and BW (5 km and 12 km south) show velocities greater than 4000 m/s (Flinchum, Holbrook, Rempe, et al., 2018). The lack of velocities greater than 4000 m/s suggests that we only observe unfractured bedrock under L10 (Figure 2). The lack of bedrock is not necessarily a function of our profile lengths since the smallest profiles were still 140 m long and previous work images bedrock with similar profile lengths (Flinchum, Holbrook, Rempe, et al., 2018; Uecker et al., 2023). The low velocities (<1200 m/s) suggest that the material at the top part of the drainage is weathered and likely has 25-35% porosities based on samples from BW (Flinchum, Holbrook, Grana, et al., 2018).

Given the similar climate, similar lithology, and similar relief, we assume that the water table is similarly flat at V1 (e.g., deeper under ridges and shallow under valleys). If an increase in saturation caused the increase in velocity, we would observe higher (Vp > 1500 /s) velocities below the elevation of the valleys under the ridges (Figure 2). Second, the water table and saprolite boundary were co-located at the BW based on six kilometers of seismic refraction data, eight boreholes, 13 Geobrobe samples, and surface and nuclear magnetic resonance soundings. The surface and borehole NMR showed perched water tables in topographic depressions in the fractured bedrock topography (see Fig. 11 in (Flinchum et al., 2019)). Recently, data from BW was imaged with full waveform inversions, showing that the saprolite and fractured bedrock boundary is sharp but laterally heterogeneous (Eppinger et al., 2024). Given the proximity, shared climates and lithologies, and identical geophysical tools used to characterize the CZ at

215 both sites, we assume a similar interpretation: velocities more significant than 1200 m/s indicate
216 fractured bedrock and not necessarily fully saturated saprolite and the water table is near the
217 vertically sharp but laterally heterogeneous boundary.

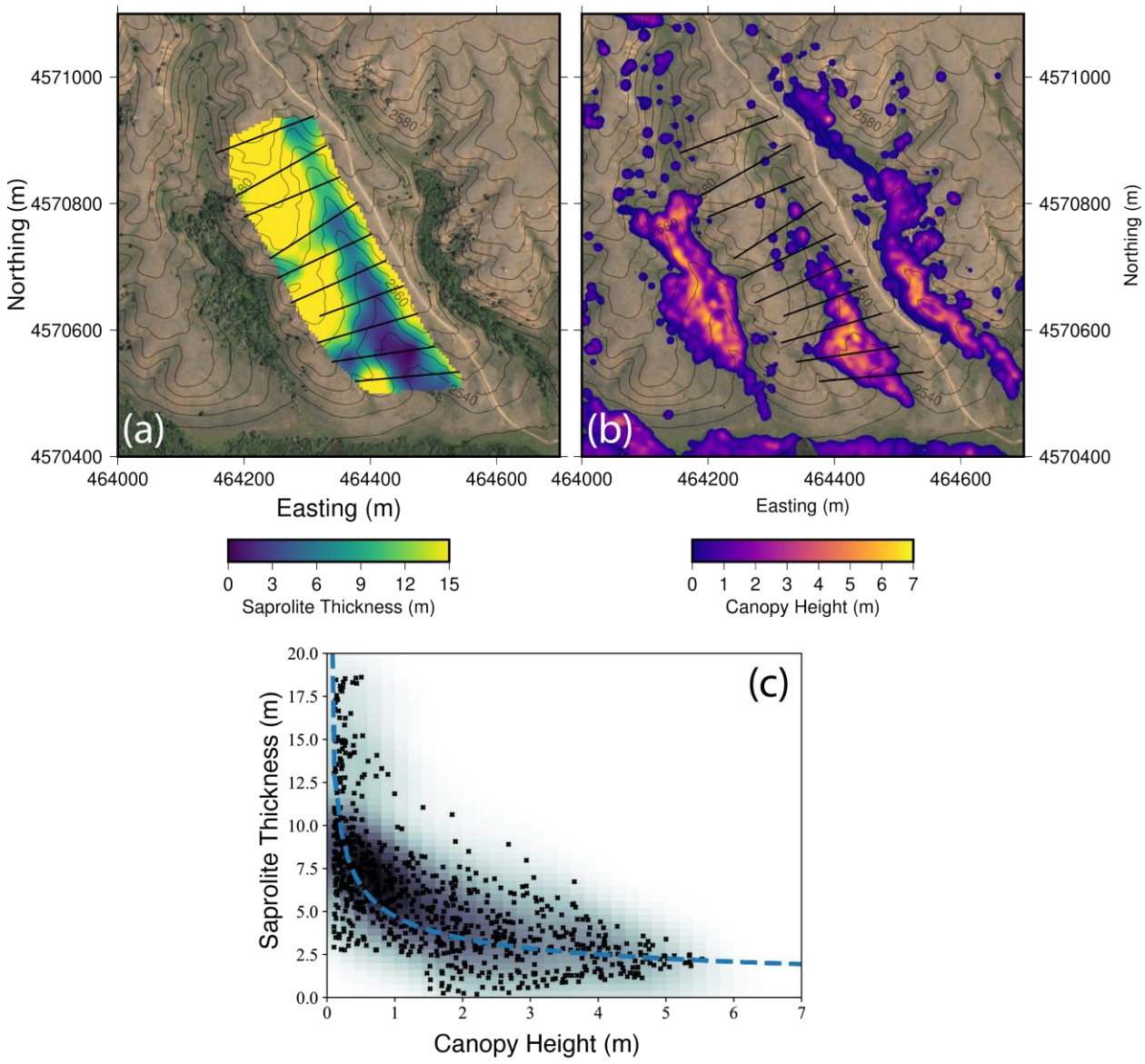

Figure 3. Saprolite thickness and canopy heights. (a) Interpolated depth to saprolite (Vp = 1200 m/s). The seismic refraction profiles are shown as thick black lines. 5 m topographic contours are also shown. (b) Canopy height after being passed through a 7x7 m smoothing filter. (c) Scatter plot of vegetation height (panel b) versus saprolite thickness (panel a). The 2D probability density function is a color map behind the data points. The blue dashed line is the power law fit ($y = ax^b; a = 4.72; b = -0.46$; R^2 = 0.47). (d) Saprolite thickness from the Blair

Wallis site 12 km south derived from seismic refraction lines. This is modified from Figure 12a in Flinchum et al. (2018).

4 Discussion

Much of the vegetation visible in the NAIP imagery is created by trees (Figure 1). Trees play an essential role in CZ development by connecting the atmosphere and the soil (Susan L. Brantley et al., 2017). They drive energy, water, and nutrient cycles that shape the CZ and soils over geologic timescales (Gabet & Mudd, 2010; Pawlik et al., 2016). In granitic landscapes that share climate, the phosphorus in the underlying bedrock is correlated with tree density, suggesting that trees may preferentially locate themselves near bedrock where they can access critical limiting nutrients (Hahm et al., 2014). The connection between tree density and underlying lithology and soil properties is well studied; for example, in Spain, elevation and lithology are the two variables that best predict maritime pine growth potential (Eimil-Fraga et al., 2014). In the southern Appalachians, depth to bedrock is a reliable predictor of forest productivity, as shallow bedrock confines the root systems of trees to a thin layer of topsoil (Carter et al., 2000). Similarly, bedrock composition (e.g. porosity, nutrient content) has been shown to influence the susceptibility of trees to water stress, especially in areas that experience periodic droughts (Callahan et al., 2022).

In addition to nutrient limitations, there is a strong connection between vegetation patterns and water availability (Banks et al., 2009; Chiloane et al., 2022; Jones et al., 2020). Evapotranspiration from stomatal pores in leaves, driven by the relatively low vapor pressure of air, creates suction – passively drawing water from the soil and into and through the xylem tissues in roots, stems and leaves (Lambers et al., 2008). Water's movement depends upon evapotranspiration's ability to generate enough negative pressure to overcome the gravitational potential and the matric potential of water held tightly in soil pores (Lambers et al., 2008). For non-wetland tree species, it is critical that the rooting zone not be fully saturated because the

stems of these species typically lack specialized aerenchyma tissues to transmit oxygen from above ground and thus must rely on oxygen from soil pores to satisfy their belowground respiratory demands (Koch et al., 2004). Therefore, for certain species to survive, many require easy access to water (e.g., well-drained soils) but cannot stay if they remain saturated year-round.

In forested uplands, tree roots are confined to the first few meters of the CZ (Canadell et al., 1996; Fan et al., 2017; Jackson et al., 1996); but recent work also shows they depend on deeper water in the fractured rock to survive long summers (McCormick et al., 2021; Rempe & Dietrich, 2018; Salve et al., 2012) and there are documented connections between vegetation density and hillslope stream connectivity (Emanuel et al., 2014). Regions of topographic convergence are usually associated with groundwater-dependent ecosystems because they are discharge zones that have the most impact on nutrient and water availability (Tai et al., 2020). This dependence on groundwater is well known, and many studies have investigated groundwater-dependent ecosystems (Chiloane et al., 2022). Trees' dependence on water has made it possible to use tree height as a metric to predict groundwater depth (Yang et al., 2019). Since the underlying CZ structure substantially impacts local groundwater flow paths, the presence or lack of trees could be used to predict the underlying CZ structure because they mark locations where conditions are optimal for their survival.

The stands of trees must have access to nutrients and water. The re-direction of water by bedrock is 3-dimensional, which is difficult to convey but is essential for a complete understanding of the system (Figure 4). In the north-south-oriented V1 drainage, the subsurface topographic gradients suggest that flow direction is primarily down the drainage (e.g., N/S flow perpendicular to the seismic profiles) rather than laterally from the ridges to the valley (i.e., E/W flow along the seismic profiles). Lateral flow into V1 and the surrounding valleys would only

occur if the water table were high enough under the ridges. In the small watershed where the trees are located, most water would travel from the north to the south before being redirected at the valley outlet to the west to flow along the regional topographic gradient out of the Laramie Range (Figure 1a). Our seismic data suggest that the fractured bedrock rises near the surface abruptly starting at L10, coinciding with the trees' beginning (Figure 2). This interpreted decrease in porosity and permeability under the valley would cause groundwater traveling from the north to the south to be directed toward the land surface.

The importance of bedrock in controlling vegetation distribution has been observed elsewhere. Different lithologies, such as large sandstone blocks embedded into a mélange, have different CZ thicknesses and thus different water storage capabilities, resulting in dramatic visual differences in vegetation distribution in California (Hahm et al., 2019). Additionally, more and more observations, both remote sensed (McCormick et al., 2021) and local measurements (Schmidt & Rempe, 2020), show that trees depend on, and thus access, water stored in the fractured rock layer below the soil—which has recently been termed rock moisture (Rempe & Dietrich, 2018; Salve et al., 2012).

In the Laramie range, the presence of trees decreases the wind velocity, allowing snow to pile up in the stands while reducing the incoming solar radiation by shading the snowpack (He et al., 2019). Thus, snow accumulates in the valley bottoms, especially in those valley bottoms with stands of trees. The presence of shallow fractured bedrock impacts water availability in two ways (Figure 4). First, the low permeability and porosity under the valley bottoms would restrict regional or local groundwater flow to shallow depths at the valley bottoms (perhaps even exfiltrating there), where it could be accessed by the trees (Figure 4). Second, fractured bedrock typically has a minor drainable porosity, so less recharge is needed to raise the water table within

297 the fractured rock. This would result in a higher water table and thus more available to plants
298 despite the semi-arid conditions. Thus, the initial pulse of snowmelt would effectively behave
299 similarly to a perched aquifer, providing the most water in well-drained soils during the peak of
300 the growing season. Then, the CZ architecture re-directs local north-south flow upward into the
301 valley, providing groundwater to sustain the trees in the late summer (Figure 4).

302 Further evidence of the influence of the bedrock on water availability is given by the
303 presence of a saturated bog along L14 from 55 to 105 and 35 m to 120 m along L13 in mid-
304 summer (recorded in the field notes by the team in late July) (Figure 2). This bog is unlikely to
305 be due to low permeability surface soils. Infiltration tests in sagebrush-covered areas (mostly
306 hilltops) throughout the Laramie Range have shown that overland flow under natural conditions
307 is rare because of the high infiltration capacity of the soils (Carey & Paige, 2016). The strong
308 association between the trees and the presence of a bog in mid-summer suggests that the deeper
309 CZ architecture is responsible for providing water and nutrients required by the trees. In
310 particular, Quaking aspen is a highly water-demanding species that grows best in porous, well-
311 drained soils with water tables between 0.6 and 2.5 m (Perala et al., 1990). Additionally, its
312 seeds, which are dispersed in late spring/early summer, require a period of contact with heavily
313 saturated soils to germinate (Perala et al., 1990). The high water demand and the need for wet
314 soils to grow suggest they would not thrive in a semi-arid environment that favors shrub or
315 grassland vegetation. However, the deep CZ structure has provided the right conditions,
316 suggesting that aspen might serve as an “indicator species” (see Clements, 1924) that could be
317 used to estimate saproilte thickness.

318 Figure 4Figure 3Figure 3Figure 3Figure 3Figure 3

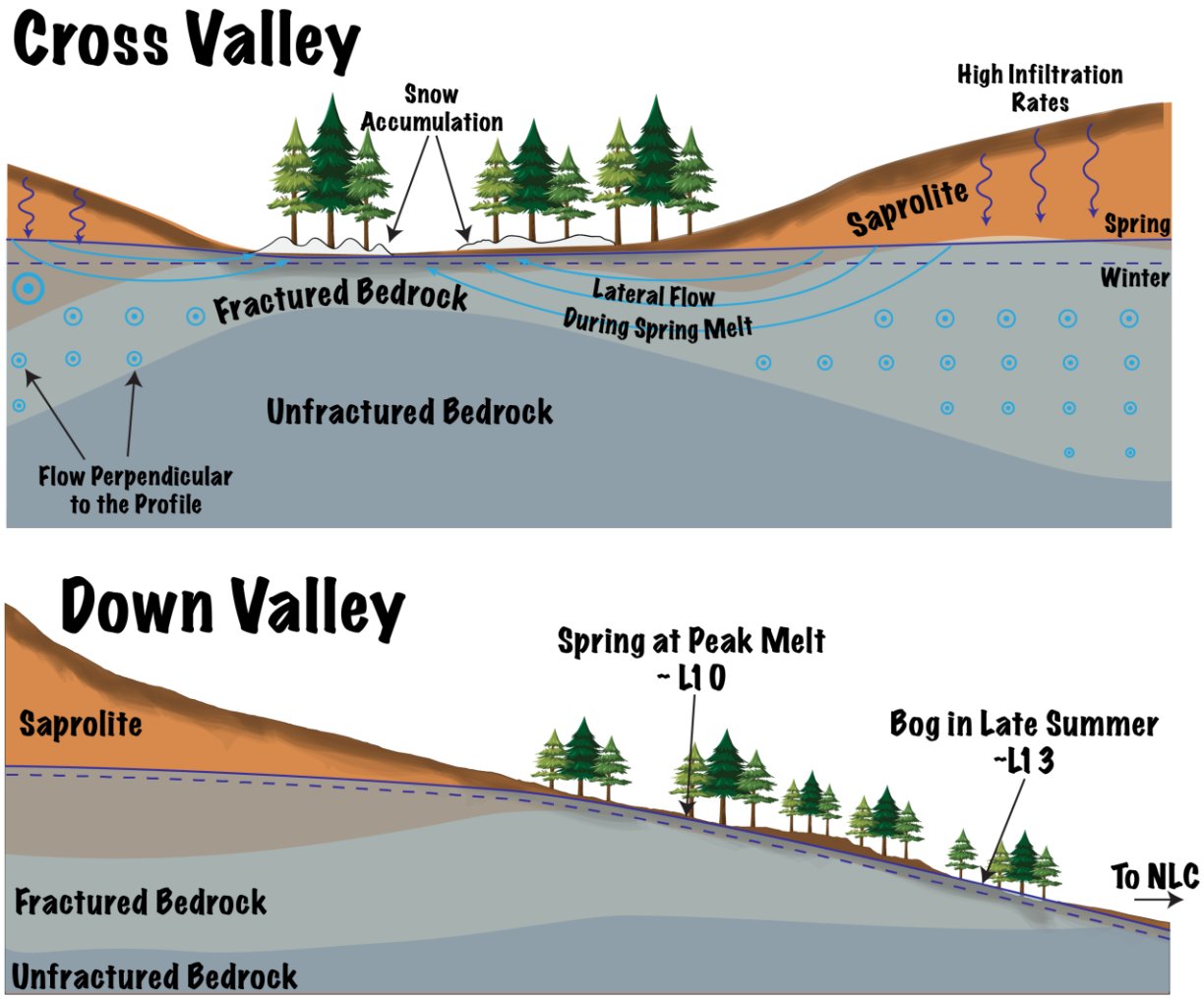

Figure 4 CZ and hydrological conceptualization, both sections are vertically exaggerated and not to scale. (a) Cross-section across the valley based on L13 from Figure 2. In the cross-section view, the water flowing perpendicular to the page is dominant, especially in the winter. The water table rises during spring melt, during lateral flow to the trees, and the shallow fractured bedrock keeps the snow melt close to the trees during the spring. (b). Down valley view.

5 Conclusions

The results presented here provide a unique perspective on the complex connections between vegetation distribution and deep CZ architecture. Our data suggest that the trees in the Laramie Range are restricted to areas with thinner saprolite. We argue that the shallow fractured bedrock structure would impact the local and regional groundwater flow patterns that would work to the advantage of the trees. The power law displayed in our data ($R^2 = 0.47$) is more evidence to suggest that in addition to other factors such as slope, aspect, and climate, the deep CZ structure plays a vital role in ecosystem development and resilience. Our results also support the idea of trees as "indicator species" for deep CZ architecture, as their presence and size reflect a unique combination of environmental and CZ factors that otherwise require sophisticated and/or labor-intensive techniques to measure. The results highlight the importance of dynamic and complex connections between ecosystem development, the underlying geology, and deep (> 5 m) CZ architecture. Although more work can be done to ground truth in the geophysical data, the spatially exhaustive observations created by seismic refraction can provide observational data of CZ structures over large areas to help our understanding of CZ processes.

Acknowledgments

We are grateful to the many undergraduate researchers who helped collect the seismic refraction data for this project as part of the Wyoming Center for Environmental Hydrology and Geophysics (WyCEHG) team under the guidance of Matthew Provart, Bradley J. Carr, and W. Steven Holbrook. We are also grateful to the broader CZ community for providing stimulating conversations over many years that have helped shape the narrative of this manuscript—specifically connecting the deep and often inaccessible CZ to observations we can make on the

surface. This study was supported by the National Science Foundation award “Collaborative Research: Network Cluster: Bedrock controls on the deep critical zone, landscapes, and ecosystems” (NSFEAR 2012357, NSFEAR 2012227, NSFEAR 2012353) and “Water in a Changing West: The Wyoming Center for Environmental Hydrology and Geophysics” (NSFEPS 1208909). Data used for this manuscript can be found and downloaded on Hydroshare:

Open Research

The data used for this manuscript can be found and downloaded on Hydroshare: Flinchum, B. A. (2024). Supporting Data Repository for Sensing a Connection: Tree Distribution is Influenced by Deep Critical Zone Structure, HydroShare, http://www.hydroshare.org/resource/56d30051589b4a5ca0cbb146eae711d3

References

Arvin, L. J., Riebe, C. S., Aciego, S. M., & Blakowski, M. A. (2017). Global patterns of dust and bedrock nutrient supply to montane ecosystems. *Science Advances*, *3*(12), eaao1588. https://doi.org/10.1126/sciadv.aao1588

Brantley, S. L., White, T. S., Sparks, D. L., Richter, D. D., Pregitzer, K. S., Derry, L. A., et al. (2005). *Frontiers in Exploration of the Critical Zone: Report of a workshop sponsered by the National Science Foundation (NSF)* (p. 30).

Brantley, Susan L. (2010). Rock to regolith. *Nature Geoscience*, *3*(5), 305–306. https://doi.org/10.1038/ngeo858

Brantley, Susan L., Goldhaber, M. B., & Ragnarsdottir, K. V. (2007). Crossing Disciplines and Scales to Understand the Critical Zone. *Elements*, *3*(5), 307–314. https://doi.org/10.2113/gselements.3.5.307

Callahan, R. P., Riebe, C. S., Pasquet, S., Ferrier, K. L., Grana, D., Sklar, L. S., et al. (2020). Subsurface Weathering Revealed in Hillslope-Integrated Porosity Distributions. *Geophysical Research Letters*, *47*(15). https://doi.org/10.1029/2020gl088322

Carey, A. M., & Paige, G. B. (2016). Ecological Site-Scale Hydrologic Response in a Semiarid Rangeland Watershed. *Rangeland Ecology & Management*, *69*(6), 481–490. https://doi.org/10.1016/j.rama.2016.06.007

Carey, A. M., Paige, G. B., Carr, B. J., Holbrook, W. S., & Miller, S. N. (2019). Characterizing hydrological processes in a semiarid rangeland watershed: A hydrogeophysical approach. *Hydrological Processes*, *33*(5), 759–774. https://doi.org/10.1002/hyp.13361

Chapin, C. E., & Kelley, S. A. (1997). Chapin and Kelley - 1997 - The Rocky Mountain erosion surface in the front ra.pdf. Retrieved from http://archives.datapages.com/data/rmag/geohistfrontrange1997/chapin_b.pdf

Dethier, D. P., Ouimet, W., Bierman, P. R., Rood, D. H., & Balco, G. (2014). Basins and bedrock: Spatial variation in 10Be erosion rates and increasing relief in the southern Rocky Mountains, USA. *Geology*, *42*(2), 167–170. https://doi.org/10.1130/g34922.1

Donaldson, A. M., Zimmer, M., Huang, M. -H., Johnson, K. N., Hudson-Rasmussen, B., Finnegan, N., et al. (2023). Symmetry in Hillslope Steepness and Saprolite Thickness Between Hillslopes With Opposing Aspects. *Journal of Geophysical Research: Earth Surface*, *128*(7). https://doi.org/10.1029/2023jf007076

Eggler, D. H., Larson, E. E., & Bradley, W. C. (1969). Granites Grusses and Sherman Erosion Surface Southern Laramie Range Colorado-Wyoming. *American Journal of Science*, *267*(4), 510-.

Emanuel, R. E., Hazen, A. G., McGlynn, B. L., & Jencso, K. G. (2014). Vegetation and topographic influences on the connectivity of shallow groundwater between hillslopes and streams. *Ecohydrology*, *7*(2), 887–895. https://doi.org/10.1002/eco.1409

401 Evanoff, E. (1990). Early Oligocene paleovalleys in southern and central Wyoming: Evidence of
402 high local relief on the late Eocene unconformity. *Geology*, *18*(5), 443–446. Retrieved from
403 http://geology.gsapubs.org/content/18/5/443.short

404 Flinchum, B. A., Holbrook, W. S., Rempe, D., Moon, S., Riebe, C. S., Carr, B. J., et al. (2018).
405 Critical Zone Structure Under a Granite Ridge Inferred From Drilling and Three-Dimensional
406 Seismic Refraction Data. *Journal of Geophysical Research: Earth Surface*, *123*(6), 1317–
407 1343. https://doi.org/10.1029/2017jf004280

408 Flinchum, B. A., Holbrook, W. S., Grana, D., Parsekian, A. D., Carr, B. J., Hayes, J. L., & Jiao,
409 J. (2018). Estimating the water holding capacity of the critical zone using near-surface
410 geophysics. *Hydrological Processes*, *32*(22), 3308–3326. https://doi.org/10.1002/hyp.13260

411 Flinchum, B. A., Holbrook, W. S., Parsekian, A. D., & Carr, B. J. (2019). Characterizing the
412 Critical Zone Using Borehole and Surface Nuclear Magnetic Resonance. *Vadose Zone*
413 *Journal*, *18*(1), 1–18. https://doi.org/10.2136/vzj2018.12.0209

414 Flinchum, B. A., Holbrook, W. S., & Carr, B. J. (2022). What Do P-Wave Velocities Tell Us
415 About the Critical Zone? *Frontiers in Water*, *3*, 772185.
416 https://doi.org/10.3389/frwa.2021.772185

417 Gillieson, D., Wallbrink, P., & Cochrane, A. (1996). Vegetation change, erosion risk and land
418 management on the Nullarbor Plain, Australia. *Environmental Geology*, *28*(3), 145–153.
419 https://doi.org/10.1007/s002540050087

Graham, R. C., Anderson, M. A., Sternberg, P. D., Tice, K. R., & Schoeneberger, P. J. (1997). Morphology, Porosity, and Hydraulic Conductivity of Weathered Granitic Bedrock and Overlying Soils. *Soil Science Society of America Journal*, *61*(2), 516. https://doi.org/10.2136/sssaj1997.03615995006100020021x

Gu, X., Heaney, P. J., Reis, F. D. A. A., & Brantley, S. L. (2020). Deep abiotic weathering of pyrite. *Science*, *370*(6515), eabb8092. https://doi.org/10.1126/science.abb8092

Hahm, W. J., Riebe, C. S., Lukens, C. E., & Araki, S. (2014). Bedrock composition regulates mountain ecosystems and landscape evolution. *Proceedings of the National Academy of Sciences*, *111*(9), 3338–3343. https://doi.org/10.1073/pnas.1315667111

Hahm, W. J., Rempe, D. M., Dralle, D. N., Dawson, T. E., Lovill, S. M., Bryk, A. B., et al. (2019). Lithologically Controlled Subsurface Critical Zone Thickness and Water Storage Capacity Determine Regional Plant Community Composition. *Water Resources Research*, *55*(4), 3028–3055. https://doi.org/10.1029/2018wr023760

Hayes, J. L., Riebe, C. S., Holbrook, W. S., Flinchum, B. A., & Hartsough, P. C. (2019). Porosity production in weathered rock: Where volumetric strain dominates over chemical mass loss. *Science Advances*, *5*(9), eaao0834. https://doi.org/10.1126/sciadv.aao0834

He, S., Ohara, N., & Miller, S. N. (2019). Understanding subgrid variability of snow depth at 1-km scale using Lidar measurements. *Hydrological Processes*, *33*(11), 1525–1537. https://doi.org/10.1002/hyp.13415

439 Holbrook, W. S., Riebe, C. S., Elwaseif, M., Hayes, J. L., Basler-Reeder, K., Harry, D. L., et al.
440 (2014). Geophysical constraints on deep weathering and water storage potential in the
441 Southern Sierra Critical Zone Observatory. *Earth Surface Processes and Landforms, 39*(3),
442 366–380. https://doi.org/10.1002/esp.3502

443 Huang, M., Hudson-Rasmussen, B., Burdick, S., Lekic, V., Nelson, M. D., Fauria, K. E., &
444 Schmerr, N. (2021). Bayesian Seismic Refraction Inversion for Critical Zone Science and
445 Near-Surface Applications. *Geochemistry, Geophysics, Geosystems, 22*(5).
446 https://doi.org/10.1029/2020gc009172

447 Keifer, I., Dueker, K., & Chen, P. (2019). Ambient Rayleigh wave field imaging of the critical
448 zone in a weathered granite terrane. *Earth and Planetary Science Letters, 510,* 198–208.
449 https://doi.org/10.1016/j.epsl.2019.01.015

450 Lebedeva, M. I., Fletcher, R. C., Balashov, V. N., & Brantley, S. L. (2007). A reactive diffusion
451 model describing transformation of bedrock to saprolite. *Chemical Geology*, *244*(3–4), 624–
452 645. https://doi.org/10.1016/j.chemgeo.2007.07.008

453 Leone, J. D., Holbrook, W. S., Riebe, C. S., Chorover, J., Ferré, T. P. A., Carr, B. J., & Callahan,
454 R. P. (2020). Strong slope-aspect control of regolith thickness by bedrock foliation. *Earth*
455 *Surface Processes and Landforms*. https://doi.org/10.1002/esp.4947

456 Marston, R. A. (2010). Geomorphology and vegetation on hillslopes: Interactions, dependencies,
457 and feedback loops. *Geomorphology*, *116*(3–4), 206–217.
458 https://doi.org/10.1016/j.geomorph.2009.09.028

McCormick, E. L., Dralle, D. N., Hahm, W. J., Tune, A. K., Schmidt, L. M., Chadwick, K. D., & Rempe, D. M. (2021). Widespread woody plant use of water stored in bedrock. *Nature*, *597*(7875), 225–229. https://doi.org/10.1038/s41586-021-03761-3

Navarre-Sitchler, A., Brantley, S. L., & Rother, G. (2015). How Porosity Increases During Incipient Weathering of Crystalline Silicate Rocks. *Reviews in Mineralogy and Geochemistry*, *80*(1), 331–354. https://doi.org/10.2138/rmg.2015.80.10

Pasquet, S., Wang, W., Chen, P., & Flinchum, B. A. (2021). Multiwindow weighted stacking of surface-wave dispersion. *GEOPHYSICS*, *86*(2), EN39–EN50. https://doi.org/10.1190/geo2020-0096.1

Pedrazas, M. A., Hahm, W. J., Huang, M., Dralle, D., Nelson, M. D., Breunig, R. E., et al. (2021). The Relationship Between Topography, Bedrock Weathering, and Water Storage Across a Sequence of Ridges and Valleys. *Journal of Geophysical Research: Earth Surface*, *126*(4). https://doi.org/10.1029/2020jf005848

Rempe, D. M., & Dietrich, W. E. (2018). Direct observations of rock moisture, a hidden component of the hydrologic cycle. *Proceedings of the National Academy of Sciences*, *115*(11), 2664–2669. https://doi.org/10.1073/pnas.1800141115

Rücker, C., Günther, T., & Wagner, F. M. (2017). pyGIMLi: An open-source library for modelling and inversion in geophysics. *Computers & Geosciences*, *109*, 106–123. https://doi.org/10.1016/j.cageo.2017.07.011

478 Salve, R., Rempe, D. M., & Dietrich, W. E. (2012). Rain, rock moisture dynamics, and the rapid
479 response of perched groundwater in weathered, fractured argillite underlying a steep hillslope.
480 *Water Resources Research*, *48*(11). https://doi.org/10.1029/2012wr012583

481 Schmidt, L., & Rempe, D. (2020). Quantifying Dynamic Water Storage in Unsaturated Bedrock
482 with Borehole Nuclear Magnetic Resonance. *Geophysical Research Letters*, *47*(22).
483 https://doi.org/10.1029/2020gl089600

484 Smith, W. H. F., & Wessel, P. (1990). Gridding with continuous curvature splines in tension.
485 *Geophysics*, *55*(3), 293–305. https://doi.org/10.1190/1.1442837

486 Uecker, R. K., Flinchum, B. A., Holbrook, W. S., & Carr, B. J. (2023). Mapping bedrock
487 topography: a seismic refraction survey and landscape analysis in the Laramie Range,
488 Wyoming. *Frontiers in Water*, *5*, 1057725. https://doi.org/10.3389/frwa.2023.1057725

489 Uhlig, D., & Blanckenburg, F. von. (2019). How Slow Rock Weathering Balances Nutrient Loss
490 During Fast Forest Floor Turnover in Montane, Temperate Forest Ecosystems. *Frontiers in*
491 *Earth Science*, *7*, 159. https://doi.org/10.3389/feart.2019.00159

492 Uhlig, D., Schuessler, J. A., Bouchez, J., Dixon, J. L., & Blanckenburg, F. von. (2017).
493 Quantifying nutrient uptake as driver of rock weathering in forest ecosystems by magnesium
494 stable isotopes. *Biogeosciences*, *14*(12), 3111–3128. https://doi.org/10.5194/bg-14-3111-2017

495 Wang, W., Chen, P., Keifer, I., Dueker, K., Lee, E.-J., Mu, D., et al. (2019). Weathering front
496 under a granite ridge revealed through full-3D seismic ambient-noise tomography. *Earth and*
497 *Planetary Science Letters*, *509*, 66–77. https://doi.org/10.1016/j.epsl.2018.12.038

498